ASME Journal of Turbomachinery
Online journal at:
https://asmedigitalcollection.asme.org/turbomachinery

R. D. Hine[1]
Whittle Laboratory,
University of Cambridge,
Cambridge CB3 0DY, UK
e-mail: rh725@cam.ac.uk

D. R. Cousins
Whittle Laboratory,
University of Cambridge,
Cambridge CB3 0DY, UK
e-mail: drc60@cam.ac.uk

L. Maden
Whittle Laboratory,
University of Cambridge,
Cambridge CB3 0DY, UK
e-mail: lm859@cam.ac.uk

S. J. Walker
Whittle Laboratory,
University of Cambridge,
Cambridge CB3 0DY, UK
e-mail: sjw269@cam.ac.uk

N. R. Atkins
Whittle Laboratory,
University of Cambridge,
Cambridge CB3 0DY, UK
e-mail: nra27@cam.ac.uk

S. D. Grimshaw
Whittle Laboratory,
University of Cambridge,
Cambridge CB3 0DY, UK
e-mail: sdg33@cam.ac.uk

J. V. Taylor
Whittle Laboratory,
University of Cambridge,
Cambridge CB3 0DY, UK
e-mail: jvt24@cam.ac.uk

Design and Analysis of a Liftfan for eVTOL Aircraft

Ducted liftfans provide greater hovering efficiency to electric vertical take-off and landing aircraft than open propellers of equal disk area. Liftfans are designed with minimized length to limit propulsor weight added and drag incurred during forward flight. Three challenges posed by the liftfan propulsor configuration are addressed in this paper. First, instead of a single-row propeller, liftfans require the design of a fully integrated stage. To maximize the hovering figure of merit, a non-dimensional measure of power consumption, the preliminary and 3D design variables of the rotor and splittered diffuser stator rows are optimized simultaneously using 3D computational fluid dynamics (CFD). The resulting prototype liftfan design is validated through experimental testing. Second, despite efficiency improvements during hover, liftfans sustain additional inlet distortion and drag during forward flight due to their surrounding nacelles. A low-order model is developed to investigate the maximum range for different fan designs with varying diffuser area ratios and forward flight tilt angles. Design selections are validated using full annulus, 3D CFD, and experimental wind tunnel tests. Third, as the electric motors of liftfans are mounted within the hub, fan-driven active cooling is necessary to prevent overheating. The stagnation pressure losses incurred by cooling airflow must be minimized without impeding heat transfer. Low-order models are developed to predict motor heat transfer and loss and to guide the design of a mixed-flow cooling fan. Experimental testing and 3D CFD simulations confirm that the addition of forward sweep and adoption of a high blade count can reduce cooling fan losses. [DOI: 10.1115/1.4067673]

Keywords: computational fluid dynamics (CFD), fan, compressor aerodynamic design, fluid dynamics and heat transfer phenomena in compressor, turbomachinery blading design, electric vertical take-off and landing aircraft

1 Introduction

The increasing demand for emission free air transport is driving a global market for electrified aviation. Electric vertical take-off and landing (eVTOL) aircraft open new market opportunities for short-range urban, regional, and military mobilities. However, further development is required to improve the thrust-to-power performance of electrically driven propulsors if eVTOL aircraft are to become viable.

Equation (1) defines the figure of merit [1]: the efficiency of a propulsor of given disk area (A_{in}) during hover. Ducted fan propulsors are proven to achieve a higher figure of merit than open propeller alternatives of equal disk area [2]. Noise output can also be attenuated through duct shielding and acoustic liners [2,3], while safety is increased through the containment of rotating blades.

$$\mathrm{FOM} = \frac{F_{\mathrm{fan}}^{1.5}}{\dot{W}_{\mathrm{x,fan}}\sqrt{2\rho_{\mathrm{atm}}A_{\mathrm{in}}}} \tag{1}$$

The electric ducted liftfan propulsor designed in this paper is shown in Fig. 1. This prototype uses a downstream diffuser to recover static pressure by expanding rotor exit flow, and by using integrated stators to turn flow and capture wasted swirl kinetic energy. To maximize net thrust, liftfan weight and therefore

[1]Corresponding author.

Contributed by International Gas Turbine Institute (IGTI) of ASME for publication in the Journal of Turbomachinery. Manuscript received September 4, 2024; final manuscript received November 16, 2024; published online February 17, 2025. Tech. Editor: David G. Bogard.

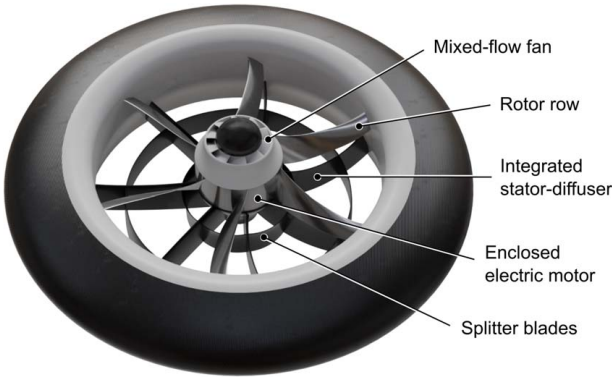

Fig. 1 Prototype ducted liftfan with splittered diffuser and upstream cooling fan

length must be minimized. However, reducing diffuser length increases the streamwise adverse pressure gradient which provokes separation. The liftfan prototype uses two axisymmetric splitter blades, designed according to Hine et al. [4], to provide control over diffuser passage loading, mitigate separation losses, and enable the use of a shorter length diffuser.

The outlet-to-inlet area ratio ($\sigma = A_{out}/A_{in}$) of the prototype is 1.28; this yields an ideal figure of merit of 1.60, assuming isentropic turbomachinery and no electrical losses. This is 60% higher than that achieved by an ideal open propeller of equal disk area, due to an increase in the cross-sectional area of the exit jet. As a result, the prototype liftfan has the potential to achieve a 37.5% reduction in power consumption during hover.

During hover, the liftfan is aligned with the vertical axis. During edge-on, forward flight, the liftfan is tilted to an angle of α° from the vertical axis, as shown in Fig. 2(*b*), so that a component of thrust is used to move in the horizontal direction. Hover is the most energy-intensive phase of eVTOL flight and is the limiting factor for application in the majority of short-range and regional use cases.

An outrunning, brushless DC motor is selected for the ducted liftfan prototype in this paper. As the electric motor is enclosed within the hub of the liftfan, the pressure difference between the inlet and exit of the liftfan is insufficient to force cooling air through the small gaps between the motor stator coils and magnetic air gap. A dedicated cooling fan is therefore required to keep the operating temperature within the limits set by the motor manufacturer. The prototype cooling fan in this paper follows the design philosophy of Smyth and Miller [5]; it exploits a centrifugal pressure rise using a mixed-flow design with an exit pitch angle of $\zeta = 65$ deg.

1.1 Liftfan Design Challenges. This paper addresses three design challenges specific to eVTOL liftfans and shows how hovering, forward flight, and cooling performance can be improved in practice. These challenges are illustrated in Fig. 2 and in this section, previous studies relating to each challenge are considered.

The first challenge is to understand the three-dimensional flows within the rotor and stator rows and how to manage them to achieve high performance. Corner separations, shown at the junctions between blades and endwalls in Fig. 2(*a*), limit the performance of the diffuser. Taylor and Miller [6] associated the presence of high loss, high blockage, open corner separations with extreme surface streamline curvature as passage loading increases. If these separations occur in the diffuser, as shown in Ref. [4], they affect the overall operating point and therefore the incidence of flow into both rotor and stator rows. The stage must be designed as a single, coupled system so that the rotor row and stator row operating points are matched.

The second challenge is to produce a design which achieves high hover efficiency without sacrificing performance during edge-on, forward flight. As illustrated in Fig. 2(*b*), flow into the fan can be distorted by separation from the inlet during forward flight, reducing lift and thrust production [7]. Lift is also exchanged for propulsive force in the freestream direction as the tilt angle is increased [8]. Zhang et al. [2] compare the streamwise propulsive efficiency of ducted and unducted propellers during axial flight as the advance ratio ($J = V_\infty/U$) increases. The advance ratio is driven by the forward flight speed (V_∞) and non-dimensionalized by the midspan rotor blade speed (U). At a low advance ratio, the duct increases efficiency by diffusing the exit jet and by mitigating tip vortices and wake mixing. However, at a high advance ratio, propulsive efficiency is reduced by additional duct drag. An operating pitch angle and advance ratio must be selected to maximize liftfan propulsive efficiency and range. The secondary effects of these parameters, on pitching moment and stall margin behavior, are outside of the scope of this paper.

Low-order modeling enables the optimization of high-level propulsor parameters with minimal computational cost. Using experimental data, Ohanian et al. [9] parameterized a non-dimensional statistical aerodynamic model for ducted fan performance in terms of the tilt angle and advance ratio. Hirono et al. [3] adopted a turbomachinery-based modeling approach: an analytic method is used to determine propulsor velocity triangles to drive the design of rotor and stator blade geometry. The forward flight analytical models developed and validated in this paper, complement these studies by using high-level design parameters to optimize ducted liftfan range.

The third challenge is to manage the heat generated by the electric motor to prevent overheating. Overheating occurs when the

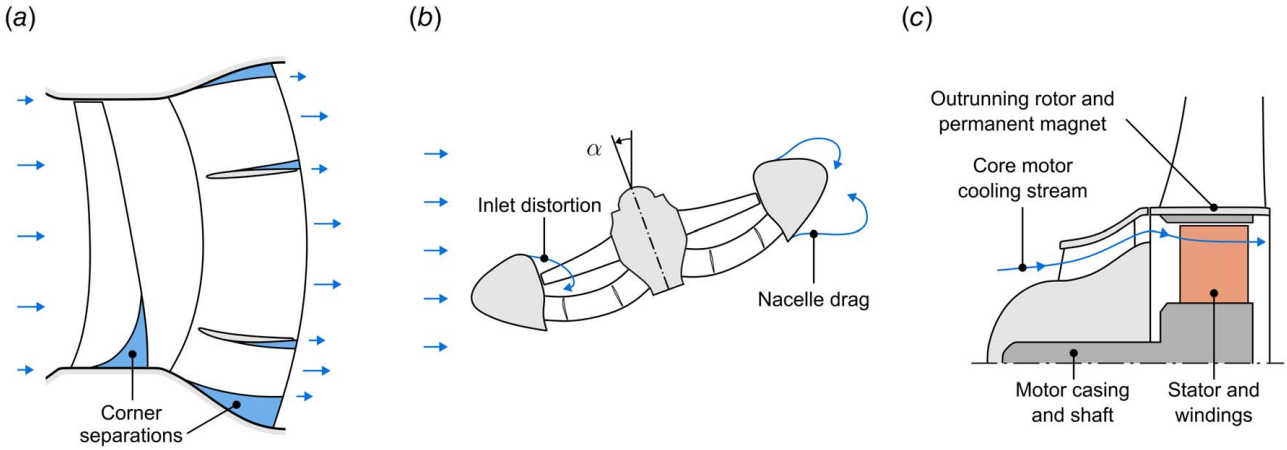

Fig. 2 Three practical design challenges that limit liftfan viability: (*a*) aerodynamics of liftfan stage with short, splittered diffuser, (*b*) external aerodynamics of liftfan operating with a tilt angle during forward flight, and (c) matching of mixed-flow cooling fan with motor aerodynamics

Table 1 Mission parameters specified for a single prototype liftfan

Thrust (F_{fan})	50.0 N
Payload mass (M_{payload})	2.00 kg
Rotor diameter (d_{c})	212 mm
Propulsor diameter	342 mm
Motor power	1050 W
Motor diameter (d_{m})	61.5 mm
Motor length (l_{m})	63.6 mm
Motor weight	0.400 kg
Temperature limit (T_{lim})	362 K

temperature of a motor exceeds the thermal limits imposed by its materials. This can reduce electrical efficiency or cause irreversible motor damage by melting wiring insulation and demagnetizing permanent magnets [10]. Motor cooling can be classified by two distinct categories: passive and active cooling. Passive cooling relies on heat dissipation through conduction, natural convection, and radiation to the environment. Active cooling systems extract heat from a motor using a forced mechanism at the expense of the added weight of machinery [11].

Automotive, electric motor active cooling is typically accomplished by pumping liquid coolant through a surrounding jacket to transport heat to a dedicated radiator [12]. However, the weight of such a system and the energy consumed by coolant pumps and radiator fans can be detrimental to eVTOL aircraft range. Hu et al. [13] fed a heat pipe from the motor windings of a ducted fan through a cooling outlet guide vane to exploit forced convection using the main gas path flow. This paper adopts a dedicated fan-driven, air-cooled, forced convection method. This approach promises to improve efficiency, reduce weight, and lower operational and maintenance costs [14].

Axial cooling fan designs are limited by insufficient pressure rise, while radial flow designs are limited by insufficient mass flow and are challenging to integrate with an internally-mounted motor [5]. Therefore, an intermediate mixed-flow compressor design is selected. The exit pitch angle (ζ) controls the degree of axial-to-radial turning. Increasing ζ produces a more radial design with a higher pressure rise. Reducing ζ produces a more axial design with a higher cooling flowrate per unit of power consumed by the fan.

1.2 Mission Design. The liftfan is designed for integration with a tilt-propulsor or quad-rotor eVTOL air vehicle [15,16], however fan-in-wing applications are also feasible [17]. The non-dimensional liftfan design methodology in this paper allows scaling for applications with any engine specification. However, a design intent is specified in Table 1 for integration of the prototype liftfan with the Greenjets Ltd. prototype, quad-rotor air vehicle shown in Fig. 3.

1.3 Multi-Order Methodology. A multi-order methodology is used to design and demonstrate the performance of the prototype liftfan in this paper. In Sec. 2, a low-order analytical model for edge-on, forward flight is used to inform preliminary liftfan design. In Sec. 3, 3D computational fluid dynamics (CFD) simulations are used to optimize the design of the main gas path turbomachinery components. In Sec. 4, 3D CFD is used to validate preliminary modeling of edge-on, forward flight and to examine non-axisymmetric flow behavior at different operating conditions. In Sec. 5, the mixed-flow, motor cooling system is developed through analytical modeling and validated using 3D CFD. Finally, in Sec. 6, a complete prototype liftfan is wind tunnel tested to validate whole system performance.

Fig. 3 Greenjets Ltd. prototype quad-rotor air vehicle

2 Forward Flight Modeling

This section describes the development of a model to evaluate liftfan aerodynamic performance during edge-on, forward flight. The model is based on the control volume defined in Fig. 4, within the reference frame of a liftfan during forward flight.

The aim of the model is to examine how eVTOL aircraft range can be optimized during preliminary design. This is achieved by reformulating the expression for non-dimensional range ($\tilde{s}$) in Eq. (2) in terms of operational parameters, such as the advance ratio and tilt angle, and geometric parameters such as the diffuser area and duct aspect ratios. Later, in Sec. 4, this model is validated with full annulus, steady CFD simulations.

$$\tilde{s} = \frac{sU^2}{\rho_{\text{E}} d_{\text{c}}} = \frac{J}{C_{\dot{\text{W}}_{\text{X}}}} \frac{M_{\text{battery}}}{\rho_{\text{atm}} A_{\text{in}} d_{\text{c}}} \tag{2}$$

The non-dimensional mass and blade speed-based Froude number terms, defined in Eq. (3) allow for the development of independent mass and aerodynamic models.

$$\widetilde{M_{\text{total}}} = \left(\frac{M_{\text{total}}}{\rho_{\text{atm}} A_{\text{in}} d_{\text{c}}} \right) \quad Fr_{\text{U}} = U/\sqrt{g d_{\text{c}}} \tag{3}$$

During forward flight, aerodynamic drag and forward thrust are balanced in the flight x-direction, as described by Eq. (4). Lift, weight, and drag components are likewise balanced in the vertical y-direction in Eq. (5).

$$C_{\text{F}_{\text{X}}} = \frac{J^2}{2} C_{\text{D}_{\text{X}}} \tag{4}$$

$$C_{\text{F}_{\text{Y}}} = \frac{\widetilde{M_{\text{total}}}}{Fr_{\text{U}}^2} + \frac{J^2}{2} C_{\text{D}_{\text{Y}}} \tag{5}$$

The steady flow momentum equations, defined by Greitzer et al. [18], are rearranged to estimate the two-dimensional thrust coefficients in Eqs. (6) and (7). Flow is assumed to be incompressible, shear forces are neglected at the inlet and exit of the liftfan, and the diffuser exit pressure is assumed to be atmospheric. The steady flow energy equation is similarly used to derive the power

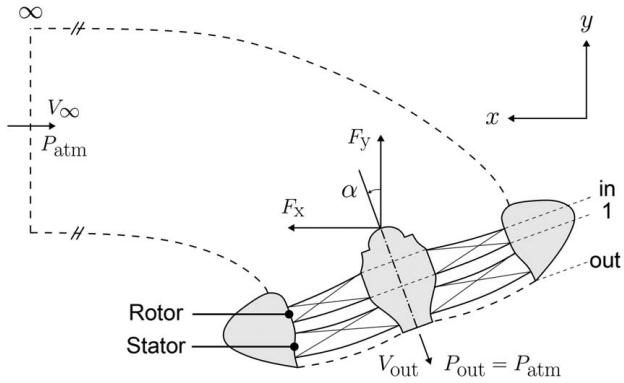

Fig. 4 Propulsor control volume and stations

coefficient in Eq. (8).

$$C_{\mathrm{F_x}} = \phi_{\mathrm{in}}\left(\frac{\phi_{\mathrm{in}}}{\sigma}\sin(\alpha) - J\right) \tag{6}$$

$$C_{\mathrm{F_y}} = \frac{\phi_{\mathrm{in}}^2}{\sigma}\cos(\alpha) \tag{7}$$

$$C_{\mathrm{W_x}} = \phi_{\mathrm{in}}\psi \tag{8}$$

Flow is assumed to be adiabatic from the freestream (∞) to rotor inlet (in) and from the rotor exit (1) to the propulsor exit (out). Bernoulli's principle is applied between the freestream and rotor row inlet to determine the required pressure rise across the rotor. This is defined by the loading coefficient in Eq. (9) and can be substituted into Eq. (8). The rotor inlet flow coefficient is defined in Eq. (10).

$$\psi = \frac{\phi_{\mathrm{in}}^2(1 - C_{\mathrm{pr}}) - J^2}{2\eta_{\mathrm{rotor}}} \tag{9}$$

$$\phi_{\mathrm{in}} = \frac{V_{\mathrm{in}}}{U} \tag{10}$$

Diffuser pressure recovery coefficients (C_{pr}) are estimated using experimental data for symmetrical annular diffusers [19]. For a diffuser of a given area ratio, the diffuser length is selected to maximize pressure recovery.

In the external flow, the liftfan is subjected to pressure drag due to the duct wake and, to a lesser extent, viscous skin drag. Reynolds number effects are assumed to be small and neglected. The streamwise drag coefficient is approximated in Eq. (11) by considering the streamwise projection of the liftfan to act as a flat plate perpendicular to the flight direction, with a drag coefficient of $f = 1.28$ [20]. This depends on the propulsor aspect ratio (l/d_{c}) and the hub-to-tip ratio through $d_{\mathrm{c}}^2/A_{\mathrm{in}}$. Due to the tilt angle, a vertical, downwards component of the drag force is also generated. This is approximated in Eq. (12) using inviscid flow theory [21].

$$C_{\mathrm{D_x}} = f\frac{d_{\mathrm{c}}^2}{A_{\mathrm{in}}}\left(\frac{\pi}{4}\sin(\alpha) + \frac{l}{d_{\mathrm{c}}}\cos(\alpha)\right) \tag{11}$$

$$C_{\mathrm{D_y}} = 2\pi\sin(\alpha) \tag{12}$$

A mass model is developed to predict the effects of changing geometric, material, and design parameters on the installed performance of liftfan designs. Equation (13) decomposes the total system mass into payload, battery, and propulsor contributions, all non-dimensionalized using $\rho_{\mathrm{atm}}A_{\mathrm{in}}d_{\mathrm{c}}$. Mission requirements determine the payload mass. The battery mass is selected using Eq. (2) depending on the desired mission range.

$$\widetilde{M_{\mathrm{total}}} = \widetilde{M_{\mathrm{payload}}} + \widetilde{M_{\mathrm{battery}}} + \widetilde{M_{\mathrm{propulsor}}} \tag{13}$$

The mass of each propulsor component, including the hub, cowling, rotor and stator blades, is expressed in a standardized form in Eq. (14). This is the product of the material density relative to air, the non-dimensional volume and a function of the rotor hub-to-tip ratio ($r_{\mathrm{h}}/r_{\mathrm{c}}$) expressed in Eq. (15). Solidity ($\gamma_{\mathrm{propulsor}}$) is used to account for the empty fraction of volume for each component.

$$\widetilde{M_{\mathrm{propulsor}}} = \gamma_{\mathrm{propulsor}}\left(\frac{\rho_{\mathrm{propulsor}}}{\rho_{\mathrm{atm}}}\right)\left(\frac{V_{\mathrm{propulsor}}}{(r_{\mathrm{c}} - r_{\mathrm{h}})^3}\right)\left(\frac{A_{\mathrm{in}}d_{\mathrm{c}}}{(r_{\mathrm{c}} - r_{\mathrm{h}})^3}\right)^{-1} \tag{14}$$

$$\frac{A_{\mathrm{in}}d_{\mathrm{c}}}{(r_{\mathrm{c}} - r_{\mathrm{h}})^3} = 2\pi\frac{1 + r_{\mathrm{h}}/r_{\mathrm{c}}}{(1 - r_{\mathrm{h}}/r_{\mathrm{c}})^2} \tag{15}$$

The x-direction momentum equation (Eq. (4)) can be reformulated to express the advance ratio as $J = J(\sigma, \alpha)$ using Eqs. (6) and (11). The y-direction momentum equation (Eq. (5)) can be reformulated to express the total system mass using Eqs. (7) and (12). The battery mass can then be obtained using Eqs. (13) and (14). Finally, by substituting the advance ratio, battery mass and power coefficient (Eq. (8)) into Eq. (2), the non-dimensional range can be expressed in the form of Eq. (16).

$$\tilde{s} = \tilde{s}(\sigma, \alpha, Fr_U) \tag{16}$$

Figure 5 shows the non-dimensional range achieved at different tilt angles and diffuser area ratios for three different non-dimensional payload masses. A modern lithium-ion battery with a specific energy density of $\rho_{\mathrm{E}} = 0.9\,\mathrm{MJ/kg}$ is assumed [22] and $Fr_{\mathrm{U}} = 56$ is selected for a high rotor efficiency without excessive blade speed. Without a payload, Fig. 5 suggests that range can be maximized by operating the liftfan at $\alpha = 25$ deg with a high diffuser area ratio of $\sigma = 1.39$. However, as the non-dimensional payload increases, the maximum range reduces and the optimal diffuser area ratio reduces toward 1. This finding has driven a conservative area ratio of $\sigma = 1.28$ to be adopted for the prototype liftfan. With this area ratio, the optimal design achieves a range of 34 km with a 6.2 kg battery shared between four liftfans.

3 Liftfan Main Gas Path Design

In this section, the main gas path turbomachinery is optimized: the rotor row and splittered diffuser row. The design with the highest figure of merit is used for the prototype.

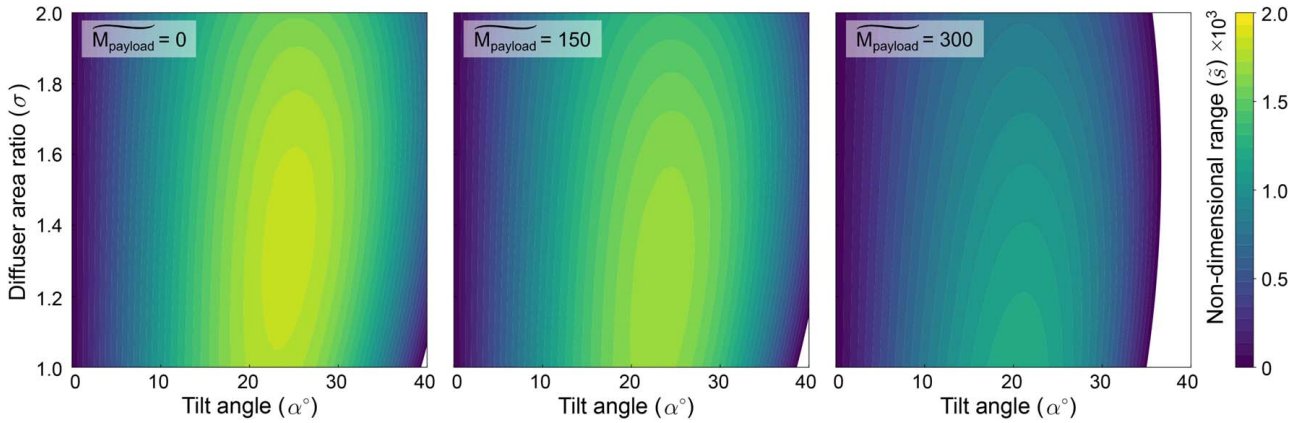

Fig. 5 Non-dimensional range achieved by datum liftfan design as tilt angle, diffuser area ratio, and non-dimensional payload mass vary

Liftfan turbomachinery is designed using a reformulation of the pattern search optimization method described in Ref. [4]. The objective function, defined in Eq. (17), is to minimize the electrical power consumed to produce the design point thrust. This function accounts for the aerodynamic efficiency of main gas path turbomachinery and the electrical efficiencies of both the motor and inverter.

$$\dot{W}_{\text{overall}} = \frac{\dot{m} c_p \Delta T_0}{\eta_{\text{motor}} \eta_{\text{inverter}}} \tag{17}$$

Turbomachinery performance is assessed using steady, single-passage CFD simulations performed using the structured, multi-block Reynolds-averaged Navier–Stokes (RANS) flow solver TURBOSTREAM 3 [23] with the Spalart–Allmaras turbulence model [24]. TURBOSTREAM 3 provides tolerance to highly non-uniform grids and rapid multi-block processing through graphics processing unit-enabled parallel computing architecture. The combined flow domain, illustrated in Fig. 6, is comprised of rotating and stationary domains, coupled using a mixing plane. This geometry is meshed using a sheared-H topology and nine blocks.

In Fig. 7, the CFD setup described in Ref. [4] is used to predict the diffuser pressure recovery coefficient, defined in Eq. (18). Hine et al. [4] described a critical non-dimensional length-to-inlet span ratio below which pressure recovery reduces rapidly due to high-loss flow separations.

$$C_{\text{pr}} = \frac{p_{\text{out}} - \overline{p_1}}{\overline{p_{0,1}} - \overline{p_1}} \tag{18}$$

The diffuser area ratio of 1.28, adopted for the liftfan prototype in this paper is more conservative than the value of 1.40 selected by Hine et al. [4]. This reduces the predicted pressure recovery coefficient. However, Fig. 7 shows that the critical length is lower for the $\sigma = 1.28$ family of diffusers than when $\sigma = 1.40$. This can be attributed to the reduced loading of blade-endwall corners. To improve robustness to uncertainty in flow conditions and error in CFD simulations, a conservative length ratio of 0.51 is also selected for the diffuser of the prototype liftfan.

The geometry of the remaining, main gas path turbomachinery is optimized using the ten parameters listed in Table 2. These include the rotor inlet flow coefficient (ϕ_{in}) and vortex exponent (nv), defined in Eqs. (10) and (19), respectively. Figure 8 also defines the pitch angles of endwalls and the fractional spanwise positions and trailing edge pitch angles of splitters. Splitter trailing edge angles are measured relative to the pitch angle of inlet flow.

$$V_{\theta \text{in}} r^{nv} = \text{constant} \tag{19}$$

The leading-edge metal angles of all blades are set to ensure zero local flow incidence and the trailing-edge metal angles of stator blades are set to ensure zero exit swirl angle. The trailing-edge metal angle of the rotor is specified to achieve the desired flow coefficient and vortex distribution. The lean and sweep angles of rotor and stator blades are set to match those found optimum by Hine et al. [4].

4 Whole Engine, Forward Flight Simulations

In this section, full annulus CFD simulations are performed on the prototype liftfan design in edge-on, forward flight. The effects of α and J on intake distortion and overall loss are observed. The assumptions made during the derivation of the low-order model in Sec. 2 are also tested.

Forward flight, CFD simulations are performed using the steady RANS flow solver TURBOSTREAM 4 [23] with the Spalart–Allmaras turbulence model [24]. The topology of the mesh is shown in Fig. 9. TURBOSTREAM 4 enables the structured block mesh described in Sec. 3 to be embedded within an unstructured mesh for flexible, automated far-field domain construction. Steady, "frozen rotor" simulations are performed using an interpolating plane between the rotor and stator domains. The flow field is evaluated across a range of tilt angles and advance ratios within the ranges $5 \text{ deg} \leq \alpha \leq 25 \text{ deg}$ and $0.1 \leq J \leq 0.5$.

The low-order, forward flight model assumes no variation of flow coefficient with advance ratio or tilt angle. Figure 10(*a*) evaluates

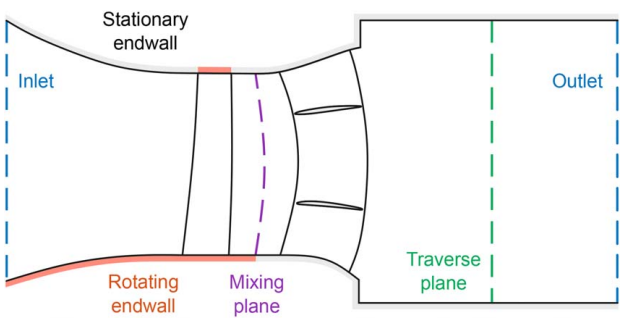

Fig. 6 Liftfan single-passage CFD domain

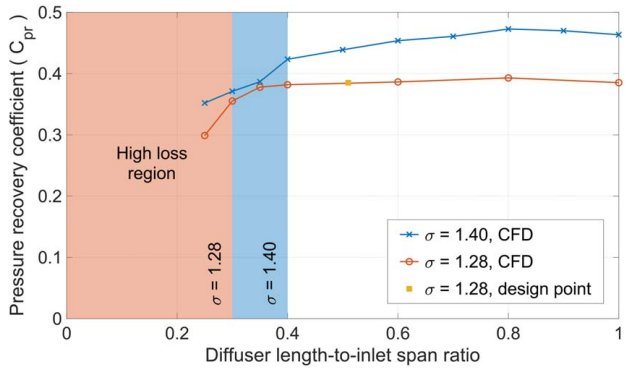

Fig. 7 Optimal pressure recovery of two-splitter, load dividing diffusers with varying lengths and area ratios

Table 2 Design parameters of optimized liftfan

Diffuser area ratio (σ)	1.28
Diffuser length-to-inlet span ratio	0.51
Rotor inlet flow coefficient (ϕ_{in})	0.60
Spanwise vortex exponent (nv)	0.10
Rotor pitch-to-chord ratio	1.6
Stator pitch-to-chord ratio	1.9
Diffuser exit hub pitch angle (β_{h})	−45 deg
Diffuser exit casing pitch angle (β_{c})	11 deg
Inner splitter, fractional spanwise position ($r_{\text{s,inner}}$)	0.28
Outer splitter, fractional spanwise position ($r_{\text{s,outer}}$)	0.76
Inner splitter, relative, exit metal angle ($\Delta\chi_{\text{s,inner}}$)	2.4 deg
Outer splitter, relative, exit metal angle ($\Delta\chi_{\text{s,outer}}$)	0.9 deg

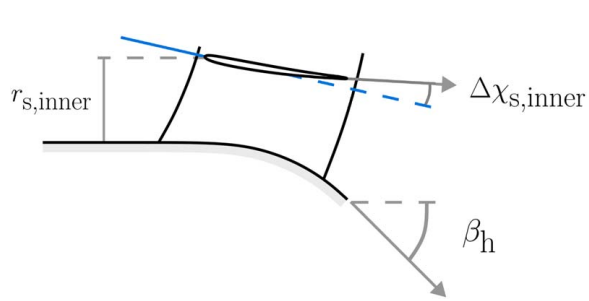

Fig. 8 Liftfan diffuser optimization parameters with reference line parallel to inlet flow

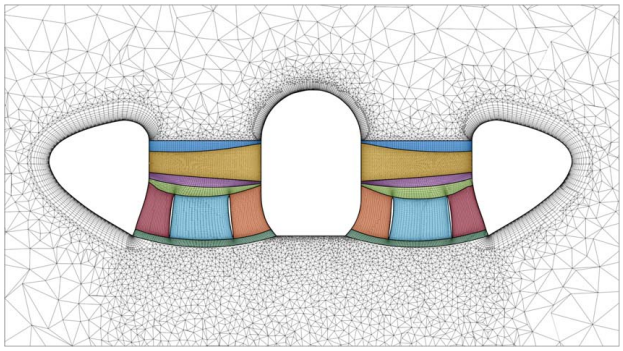

Fig. 9 Cross-sectional view of liftfan mesh topology with structured, internal mesh blocks

the flow coefficient as J and α vary, at a blade speed-based Reynolds number of $\mathrm{Re_U} = 9.5 \times 10^5$. The largest deviation from the design flow coefficient is −3.1%, suggesting that the constant flow coefficient assumption is sufficient for preliminary modeling. The model also assumes that the static pressure at the diffuser exit is atmospheric. Figure 10(*b*) shows that the greatest deviation from this assumption occurs at an advance ratio of 0.4 with a maximum that is 35% of the outlet dynamic head. This provides sufficient confidence in the application of this assumption.

Figure 11 shows instantaneous contours of non-dimensional stagnation pressure rise, defined by Eq. (20), downstream of the liftfan at varying advance ratios and tilt angles. These results demonstrate an increase in loss at $\alpha = 5$ deg as J is increased. Between Figs. 11(*a*) and 11(*b*), the size of separations from stators increases; particularly from the blades with the largest projected areas in the streamwise direction. In Fig. 11(*c*), loss is increased across the entire annulus except at the trailing side of the liftfan.

$$C_{\mathrm{p_0}} = \frac{p_{0,\mathrm{out}} - p_{0,\mathrm{in}}}{\frac{1}{2}\rho_{\mathrm{atm}} U^2} \tag{20}$$

The stagnation pressure and swirl distortion coefficients, defined in Eq. (21) [25], are based on the worst-affected, 60 deg sectors of the rotor outlet plane. These are evaluated in Fig. 12 across the full range of operating parameters. The radial and circumferential sectioning methods described in Ref. [26] are used to account for separations from the endwalls and splitters separately.

$$\mathrm{DC} = \frac{\overline{p_{0,1}} - \min(\overline{p_{0,1\ 60\,\mathrm{deg}}})}{\overline{p_{0,\mathrm{in}}} - \overline{p_{\mathrm{in}}}} \qquad \mathrm{SC} = \frac{\max(\,|\,\overline{V_{\theta,1\ 60\,\mathrm{deg}}}\,|\,)}{\overline{V_{\mathrm{x,in}}}} \tag{21}$$

Figure 12 demonstrates increased inlet distortion, in the worst affected regions of the annulus, as the advance ratio increases. This corresponds with the increase in liftfan outlet blockage observed between Figs. 11(*a*) and 11(*c*). The increase in inlet distortion due to separation from the intake promotes blockage at the diffuser outlet.

At all advance ratios, flow is seen to separate from the casing on the leading side of the liftfan. However, increasing the advance ratio between Figs. 11(*a*) and 11(*c*) is seen to reduce casing separations at the trailing side of the liftfan. The increased kinetic energy of incident flow on this side of the casing energizes the boundary layer sufficiently to limit endwall separation.

When the tilt angle is increased to $\alpha = 25$ deg, Figs. 11(*d*)–11(*f*) show that the loss due to stator separations reduces at a given advance ratio. This can be attributed to a reduction in the severity of intake separations: more flow passes through the liftfan and the incidence at stator leading edges is reduced.

At a high advance ratio, Fig. 12 suggests that stagnation pressure distortion peaks at a tilt angle of 15 deg while swirl distortion reduces as the tilt angle is increased. As a result, a reduction of diffuser outlet blockage is achieved, between Figs. 11(*c*) and 11(*f*), when increasing the tilt angle beyond 15 deg.

In this paper, a single symmetric intake geometry is studied. However, it is clear that optimization of a non-axisymmetric intake or non-axisymmetric diffuser will provide benefits during forward flight. This would help to mitigate separations, observed in Fig. 11, from the liftfan leading side and lower quadrant stator blades with minimal penalty during pure hover.

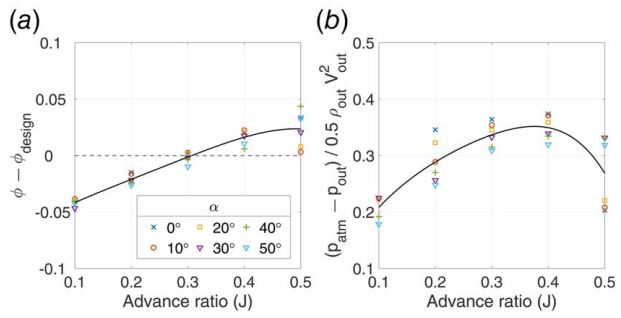

Fig. 10 Validation of low-order model assumptions across operating range with cubic fit lines

5 Mixed-Flow Cooling Fan Design

Having fixed the whole engine geometry, the remaining task is to design a cooling fan that is matched to the electric motor and the operating point of the main fan. This section describes the development of thermodynamic and aerodynamic models of flow through the motor coils. The aim of this is to inform the design of a mixed-flow cooling fan to regulate motor temperature. CFD simulations are used to identify aerodynamic loss mechanisms, to investigate the effects of scaling motor geometry and to derive constants for the low-order model.

5.1 Heat Transfer and Stagnation Pressure Loss Model.

The flowrate and pressure rise of the cooling fan must be selected to match motor heat transfer limits and pressure loss characteristics. The power output of an electric motor directly relates to the waste heat produced in the solid components and therefore the cooling flowrate required to reject heat. However, an increase in the cooling flowrate will increase stagnation pressure loss as flow is forced through narrow gaps within the motor. This drives a change in the cooling fan flow and stage loading coefficients. It is therefore essential that heat transfer from, and pressure loss through a motor, are modeled together.

Two contributions are considered when modeling the heat transfer and pressure drop across a motor. First, the motor shaft, casing, and coil front, and rear faces are modeled as bluff bodies. Second, the flow between adjacent coils is modeled as flow through a duct. Contributions are superposed under the assumption that the changes in temperature and pressure are small relative to their reference values.

Whitaker's correlation [27] for flow around a cylinder is used to model bluff body heat transfer. The bluff body stagnation pressure loss per unit frontal area is modeled by Eq. (22) using a drag coefficient of $C_D = 0.5$ corresponding to the profile of a cylinder in a regime of turbulent flow.

$$\Delta p_{0,\mathrm{bluff}} = \frac{1}{2}\rho_{\mathrm{atm}} \left(\frac{V}{2}\right)^2 C_{\mathrm{D}} \tag{22}$$

The pressure loss and heat transfer through the coils are modeled using pipe flow correlations provided by Holman [28], assuming a triangular cross section. The duct flow stagnation pressure loss is expressed in Eq. (23), where $\mathrm{Re_{duct}}$ is the duct Reynolds number based on hydraulic diameter (d_{H}), l_{duct} is the duct length, V_{duct}

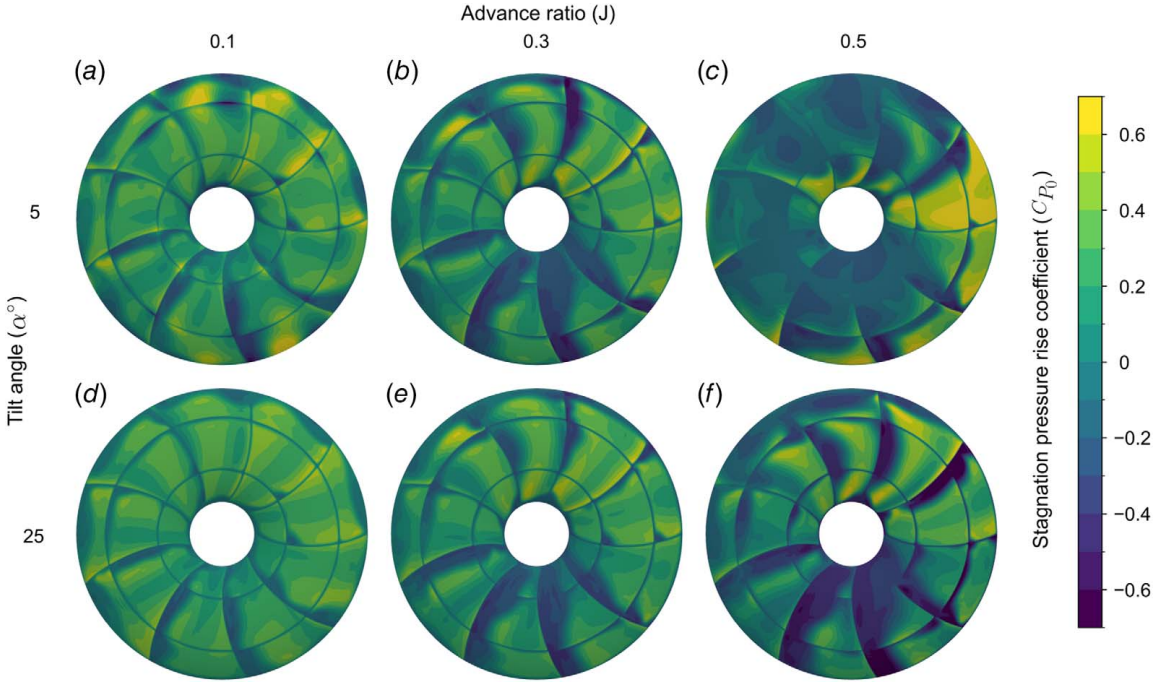

Fig. 11 Stagnation pressure rise at diffuser outlet as tilt angle and advance ratio are varied, assuming frozen rotor with edge-on, forward flight producing incident flow from left to right

is the mean velocity of the cooling flow, and n is a power law coefficient.

$$\Delta p_{0,\text{duct}} = \frac{l_{\text{duct}}}{d_{\text{H}}}\left(\frac{1}{2}\rho_{\text{atm}} V_{\text{duct}}^{n}\right)\left(1.82\log_{10}(\text{Re}_{\text{duct}}) - 1.64\right)^{-2} \tag{23}$$

5.2 Mixed-Flow Cooling Fan Model. The meridional geometry of the mixed-flow cooling fan, shown in Fig. 13, is selected by matching the stagnation pressure rise achieved by a fan design with the temperature of the motor. The work of Smyth and Miller [5] is used to derive the stagnation pressure rise coefficient of the cooling fan defined in Eq. (24) where R_2/R_3 and A_2/A_3 can be defined as functions of ζ. Setting $\xi_{3,\text{rel}} = 0\,\text{deg}$ in Eq. (24) is found to maximize the stagnation pressure rise achieved by a fan, assuming that no swirl is recovered.

$$\begin{aligned}\Psi_{\text{cf}} &= \frac{\Delta p_0}{\frac{1}{2}\rho_{\text{atm}}(R_3\Omega)^2} \\ &= 1 - Y_{\text{p}}\left(\frac{R_2}{R_3}\right)^2 - \phi_{\text{cf}}^2\left(\left(\frac{A_2}{A_3}\right)^2\tan^2\xi_{3,\text{rel}} + Y_{\text{p}}\right)\end{aligned} \tag{24}$$

The cooling fan flow coefficient is defined in Eq. (25). While Smyth and Miller [5] use R_2 for non-dimensionalization, this paper uses R_3 because it is constrained by the diameter of the liftfan motor.

$$\phi_{\text{cf}} = \frac{V_2}{R_3\Omega} \tag{25}$$

Equation (26) defines the non-dimensional, steady-state peak surface temperature of the liftfan motor. Figure 14 plots the steady-state motor temperatures achieved by the meridional cooling fan designs that achieve the highest stagnation pressure rise as the exit pitch angle varies. A design with $\zeta = 65\,\text{deg}$ is selected to maximize fan efficiency.

$$\theta = \frac{T_{\text{m}} - T_{\infty}}{T_{\text{lim}} - T_{\infty}} \tag{26}$$

Having fixed the meridional geometry, compressor blades are designed. Endwall profiles are produced by fitting cubic splines between the inlet and outlet. Blade sections are designed for controlled diffusion. The leading-edge angle of fan blades is selected to achieve zero incidence at the design point. Weisner's slip factor [29] is used to select the trailing-edge metal angle and pitch of fan blades needed to achieve the desired fan exit swirl.

5.3 Motor Cooling Flow Simulations. Steady cooling flow CFD simulations are performed using the Simcenter STAR-CCM+ RANS flow solver [30]. STAR-CCM+ provides effective multiphysics simulations, enabling prediction of both heat transfer and aerodynamic pressure losses. Flow is simulated through the gap between two stator coils within a single-passage sector with periodic boundary conditions and the Spalart–Allmaras turbulence model [24]. The Biot number of coils is found to be small ($\text{Bi} < 0.1$) so a lumped heat capacity assumption is adopted: coil temperature is assumed to be fixed and uniform, and coils are assumed to be the only heat source within the domain. To enable rapid simulation of different inlet boundary conditions, the mesh is simplified by assuming smooth coil surfaces.

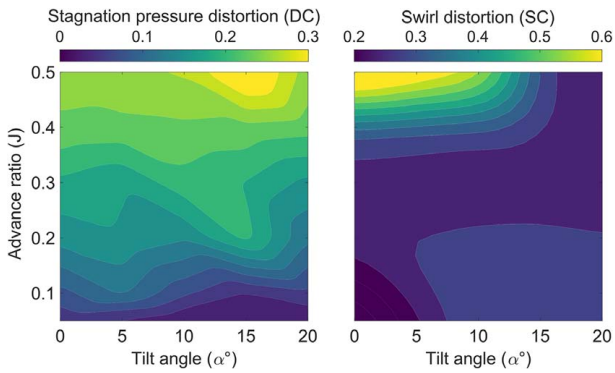

Fig. 12 Intake distortion across operating range

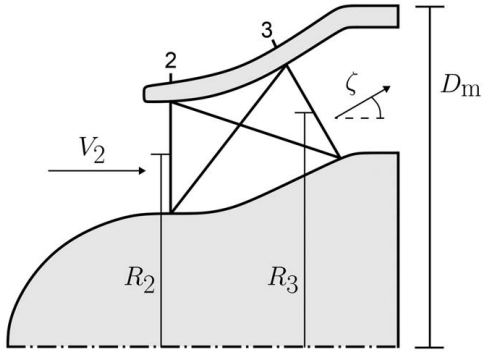

Fig. 13 Geometry of mixed-flow fans defined by Smyth and Miller's philosophy [5]

The non-dimensional groups defined in Eqs. (27)–(29) are used to characterize the cooling flowrate, heat transfer, and stagnation pressure loss, respectively.

$$\widetilde{\mathrm{Re}} = \frac{\dot{m}}{\mu d_\mathrm{m}} \tag{27}$$

$$\widetilde{\mathrm{Nu}} = \frac{\dot{m} c_\mathrm{p}}{\lambda l_\mathrm{m} N}\left(\frac{\Delta T}{T_\mathrm{m} - T_\infty}\right) \tag{28}$$

$$\widetilde{Y}_\mathrm{p} = \frac{\rho_\mathrm{atm} d_\mathrm{m}^4 \Delta p_0}{\dot{m}^2} \tag{29}$$

Stagnation pressure loss mechanisms are distinguished by mass-averaging quantities at the stations in Fig. 15. Overall pressure loss can be considered in terms of three loss mechanisms. First, duct loss is caused by viscous stresses in the flow between coils from stations b to c. Second, coil bluff body loss is caused by separated flow behind the trailing faces of the motor coils between stations c and d. Finally, the motor bluff body loss is caused by large regions of separated flow behind the motor body and the subsequent mixing out of flow between station d and the domain outlet at station e.

Figure 16 shows that approximately 50% of the total loss can be attributed to coil bluff body loss, 40% to exit bluff body loss, and 10% to duct loss. As the Reynolds number of flow increases, the loss coefficients associated with each mechanism decrease but relative contributions remain consistent.

Power-law curves are fitted in Fig. 16 to inform the low-order model. The two bluff body loss mechanisms have similar power-law exponents of $n \approx 1.7$, while that of the duct loss mechanism is $n \approx 1.4$. This reinforces the low-order model assumption that the stagnation pressure loss and heat transfer models can be treated as the superposition of two independent components: a bluff body term and a duct term.

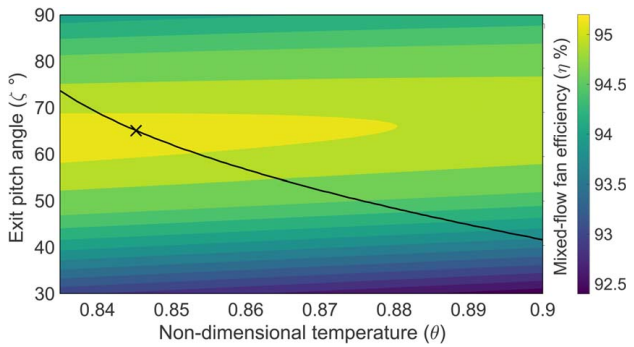

Fig. 14 Cooling fan operating line and selection of exit pitch angle (marked by cross)

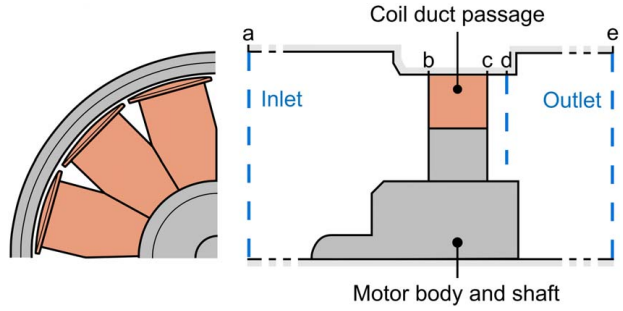

Fig. 15 Contracted motor cooling passage domain

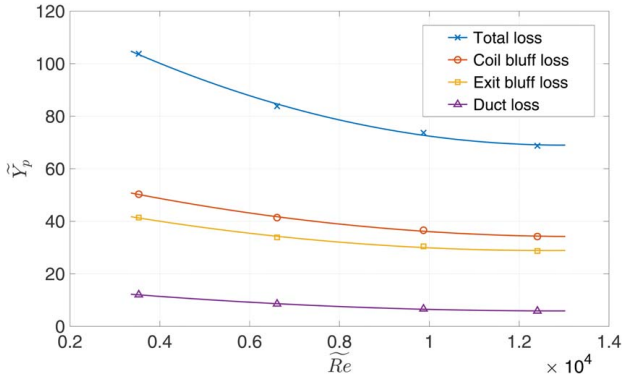

Fig. 16 Identification of sources of stagnation pressure loss from flow through the motor

All potential motor selections are collapsed to singular curves in Fig. 17 using the non-dimensional analytical model. To help tune heat transfer and stagnation pressure loss predictions across the full range of Reynolds numbers, motors of different scales are tested experimentally and using multi-physics simulations. This demonstrates that all relevant physical phenomena are captured by the selected non-dimensional groups.

5.4 Mixed-Flow Cooling Fan Simulations. Steady, single-passage cooling fan flow simulations are performed using the TBLOCK RANS flow solver, validated by Klostermeier [31]. The flow domain is shown in Fig. 18.

A parametric study is performed to improve the fan design produced by the low-order model design tool. Figure 19 compares the compressor operating characteristics of the datum and improved designs and shows the operating curve that is set by coupling the fan with the selected motor. The stagnation pressure rise is increased by reducing the pitch-to-chord ratio and adding forward sweep to the

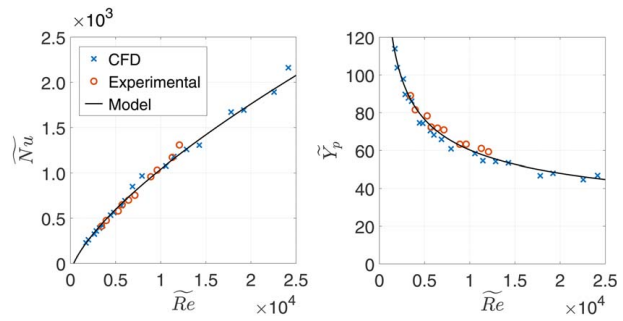

Fig. 17 Effect of motor geometric scaling on characteristic non-dimensional groups

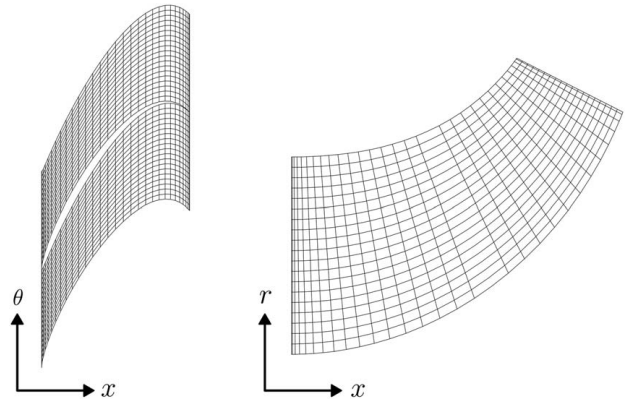

Fig. 18 Cooling fan mesh topology

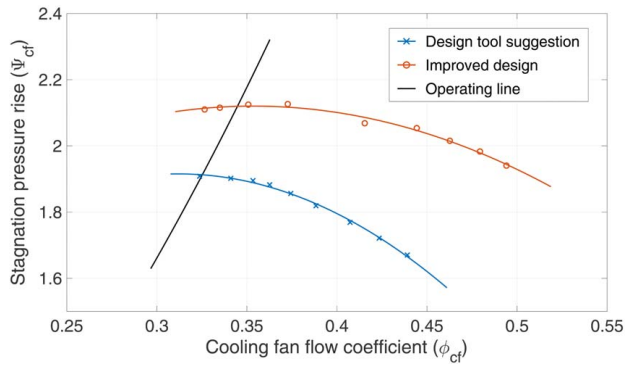

Fig. 19 Comparison of design tool output and improved cooling fan design from CFD study

trailing edges. This provides flow incidence and turning that more closely matches the design intent.

6 Experimental Prototype Testing

In this final section, a complete prototype liftfan is manufactured and wind tunnel tested. The prototype is produced through a combination of polymer additive manufacturing and five-axis aluminum alloy machining. The experimental setup is described and three sets of experimental results are presented. First, the performance of the liftfan during hover is investigated through external flow field measurements. Then, wind tunnel measurements are used to validate the low-order, forward flight model. Finally, the performance of the cooling system is evaluated when integrated with the main gas path turbomachinery. All comparisons between experimental measurements and CFD simulations are conducted using identical ambient boundary conditions.

6.1 Wind Tunnel, Propulsor Test Rig. Figure 20 illustrates the wind tunnel test rig which is used to validate the prototype liftfan. To measure the components of thrust, F_X and F_Y, the liftfan is mounted on a pair of load cells shrouded within an aerodynamic fairing. To calibrate the load cells, a series of known forces are applied and a correlation between load cell voltage and force is derived. A variable pitch mount is used to vary the tilt angle.

Upstream pitot and static pressure probes are used to measure the freestream flow speed. A pneumatic, five-hole probe mounted on a two-axis traverse system is used to measure the pressure field across the liftfan outlet plane. A 2 mm probe head diameter is selected as a compromise between settling time and measurement accuracy [32]. The probe is calibrated in 2 deg increments between pitch and yaw flow angles of ±26 deg.

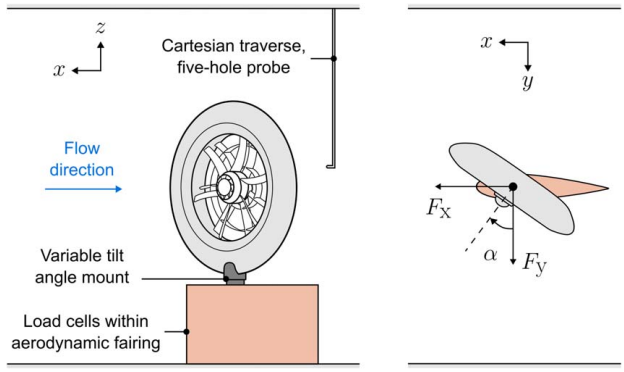

Fig. 20 Liftfan wind tunnel rig schematic

The five-hole probe is traversed across the plane defined in Fig. 6, located approximately 1.5–2 stator chord lengths downstream of the diffuser trailing edge, to capture the interaction of the exit jet with ambient air. Traverse points are clustered in the radial and circumferential directions across stator and splitter wakes. Flow is traversed across a single-passage outlet and periodicity is assumed. These measurements provide insight into the flow mechanisms at the liftfan exit. By integrating momentum flux and pressure across the traverse plane, an auxiliary measurement of streamwise thrust is also obtained to validate load cell measurements.

The liftfan is powered by a 15 kW DC supply from which power consumption is recorded. Motor temperature is monitored using a K-type thermocouple fixed to the rear face of the motor coils where the surface temperature is the greatest. Shaft rotational speed and load cell forces are also logged synchronously.

6.2 Liftfan Hover Performance. Flow is traversed at the exit of the liftfan in a stationary hover configuration. Figure 21 compares computationally predicted and experimentally measured stagnation pressure rise coefficients, defined in Eq. (20), across the traverse plane.

In the casing passage, an open corner separation is observed between the casing endwall and stator suction surface. While, the simulation correctly predicts the formation of this flow structure, the loss of stagnation pressure is under-predicted. The simulation also overestimates the peak pressure rise in the casing passage. This is likely a result of the larger corner separation mixing with the downstream jet during prototype testing.

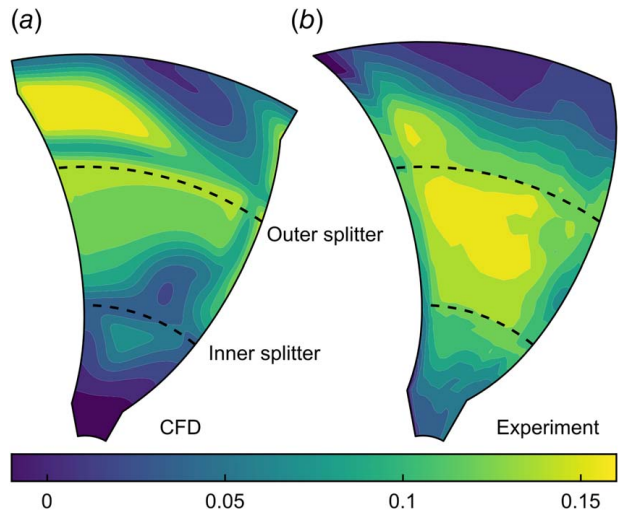

Fig. 21 Stagnation pressure rise coefficient contours in the exit jet of the Liftfan in hover: (*a*) CFD and (*b*) experiment

In the central passage, a smaller corner separation is observed between the inner splitter and the stator suction surface during simulations but not during prototype testing. The average stagnation pressure rise coefficient is 25% larger in the central passage of the experimental domain than the computational equivalent. Taylor and Miller [6] found that the opening of corner separations is sensitive to the incidence of flow. Therefore, it is possible that this difference between experimental and simulated flow behavior is caused by a small discrepancy in incidence angle. As for the casing passage, this can be attributed to downstream mixing across the corner separation.

In the hub passage, the increase of stagnation pressure is greater in the experimental contour than the computational equivalent. Discrepancies in flow incidence augment the loading of the hub passage, resulting in more severe blockage in the computational domain. Figure 21(*a*) suggests that the wakes of splitters are swept radially toward the casing. One could suggest that the deflection of the hub separation drives this radial migration.

The figure of merit, defined in Eq. (1), is assessed for the prototype liftfan. A figure of merit of 0.96 is calculated using engine thrust measurements derived from experimental flow traverses. A figure of merit of 0.72 is obtained using load cell measurements of engine thrust: a 25% reduction compared to the traverse-derived result. CFD calculations yield a figure of merit of 0.62: this is 14% lower than that obtained using experimental load cell measurements.

6.3 Validation of Forward Flight Low-Order Model. The liftfan prototype is mounted in the tunnel and measurements are taken as the rotor speed, tilt angle, and freestream flow speeds are varied. Figure 22(*a*) shows that the streamwise drag coefficient reduces as the liftfan tilt angle is reduced and as the Reynolds number $\mathrm{Re_D}$, based on flight velocity and fan diameter, is increased. However, a reduction in drag is observed as α increases from 20 deg to 30 deg. This can be attributed to an upstream shift in the location of boundary layer transition, delaying separation from the casing and reducing the size of the wake.

Figure 22(*b*) demonstrates an agreement in drag behavior between the low-order model and wind tunnel tests at low tilt angles. However, beyond $\alpha \approx 20$ deg, the model displays some underestimation of $C_{\mathrm{D_X}}$. At these extreme tilt angles, the assumption of axisymmetric flow becomes invalid, as shown in Fig. 11.

Figure 23(*a*) shows that the net streamwise force ($C_{\mathrm{F_X}} - C_{\mathrm{D_X}}$) decreases as J increases. When $J < 0.35$, increasing α increases the streamwise force by aligning the thrust vector more closely with the streamwise axis. However, when $J > 0.35$ the additional bluff body drag at higher α reduces the net force. Figure 23(*b*) extracts the operating points for constant forward flight speed: when $C_{\mathrm{F_X}} = C_{\mathrm{D_X}}$. No streamwise thrust is expected at $\alpha = 0$ deg, so $J = 0$ is the assumed operating point. Figure 23(*b*) suggests that the model underestimates the optimal advance ratio when $\alpha < 25$ deg and overestimates it when $\alpha > 25$ deg but, overall, the model provides a useful indication of liftfan performance.

Figure 24 compares experimentally measured and predicted liftfan power requirements. It suggests that when the liftfan axis is not aligned with streamwise flow ($\alpha < 90$ deg), an additional loss coefficient must be used to capture the intake separation behavior previously observed in Fig. 11. This is defined in Eq. (30) and used to modify the rotor loading coefficient in Eq. (31). $Y_{p,intake} \approx 1.22$ is calculated, using CFD simulations, when $\alpha = 10$ deg and across all advance ratios. Figure 24 demonstrates experimental agreement when this correction is applied. Input power under-prediction is due to the drag under-prediction, observed in Fig. 22.

$$Y_{\mathrm{p,intake}} = \frac{p_{0,\infty} - p_{0,\mathrm{in}}}{\frac{1}{2}\rho V_{\mathrm{in}}^2} \tag{30}$$

$$\psi = \frac{\phi^2(1 - C_{\mathrm{pr}}) - J^2(1 - Y_{\mathrm{p,intake}})}{2\eta_{\mathrm{rotor}}} \tag{31}$$

6.4 Cooling System Performance. The liftfan is tested in hover at its maximum rated speed with and without the cooling fan installed. Without cooling, Figure 25 shows that the temperature of the liftfan motor exceeds its safety limit within 50 s of operation. When cooled, the steady-state motor temperature is maintained below the safety limit. The application of this mixed-flow fan therefore allows the liftfan to be operated continuously with increased power density and a reduced risk of overheating. Testing shows that cooling fan operation does not significantly influence the mainstream flow or provoke flow separation.

6.5 Scaling Effects. The design point of the experimental prototype is defined non-dimensionally. As a result, aerodynamic

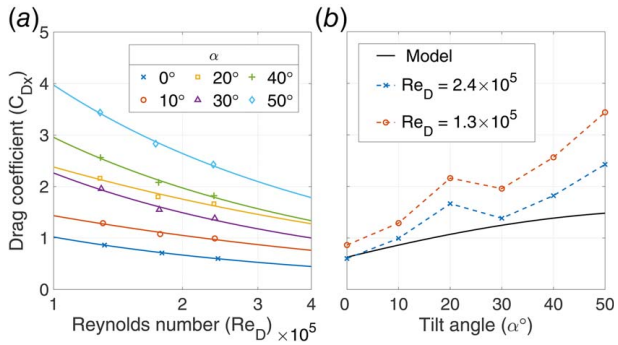

Fig. 22 Effect of Reynolds number and tilt angle on flight direction liftfan drag coefficient

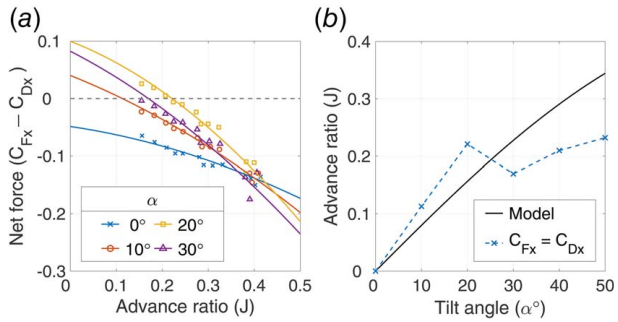

Fig. 23 Effect of advance ratio and tilt angle on liftfan net force coefficient

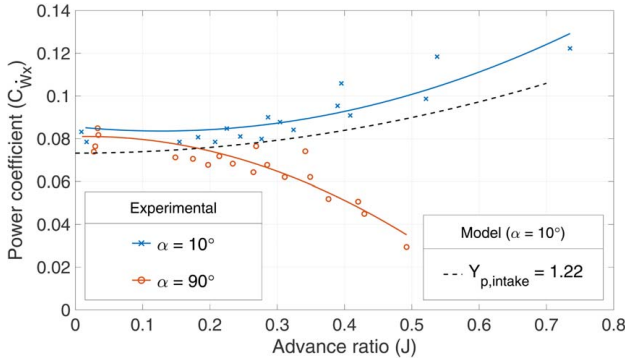

Fig. 24 Experimental input power and low-order model prediction with intake loss correction

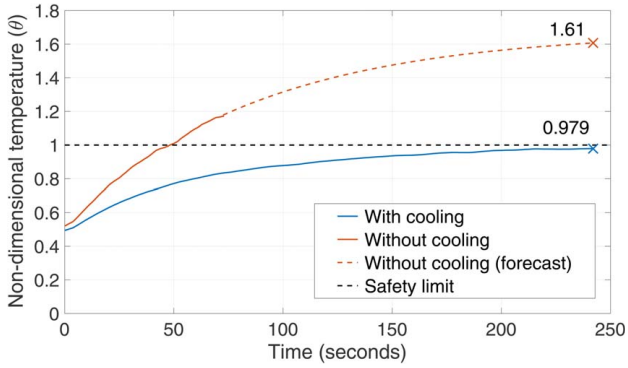

Fig. 25 Evolution of liftfan motor temperature with and without a cooling fan

surfaces can be geometrically scaled to larger propulsors, while maintaining similar non-dimensional performance values.

The Reynolds number of flow increases for larger fans, resulting in a reduction in loss and an increase in fan efficiency. This effect is, however, minimal above a chord-based Reynolds number of 1.8×10^5 [33]. Therefore, only marginal improvements in non-dimensional aerodynamic performance are expected for larger scale propulsors.

Non-dimensional cooling flow performance is expected to change at a greater rate than main gas path aerodynamic performance, as propulsor dimensions are increased. Motor power scales approximately with the cube of the blade speed so the demand for cooling rises disproportionally. To meet this demand, cooling fan geometry must be modified to accommodate increased mass flow.

7 Conclusions

A multi-order methodology has been demonstrated for the design of a novel engine configuration. Low-order analytical models are used to generate preliminary designs which inform the optimization of rotor and splittered diffuser blading using 3D CFD. Finally, a prototype is manufactured and tested to validate liftfan engine performance.

Coupled internal and external flow models for edge-on, forward flight are validated using experimental data. To maximize range, it is found to be optimal to operate the designed liftfan with a tilt angle of $\alpha = 25$ deg. Moreover, full annulus simulations suggest that operating at an advance ratio of $J = 0.4$ will mitigate the effects of inlet separation on downstream blade rows.

Heat transfer and pressure loss models for the cooling stream through an electric motor have been validated through CFD simulations. This has been used both to understand the scaling of the cooling problem to different engine sizes and to design a mixed-flow cooling fan for the liftfan prototype. During continuous experimental operation, the mixed-flow fan is shown to successfully maintain the motor temperature below the required safety limit.

Complete liftfan experiments demonstrate superior performance to the CFD predictions and a whole-system figure of merit of 0.72 is achieved in static hover, including electrical losses. This is 89% higher than the value which can be achieved by a well-designed, 330 mm diameter propeller using the same electrical system [34].

Acknowledgment

The authors would like to thank Greenjets Ltd. for their support of this work and TURBOSTREAM Ltd. for the use of their solvers. They are also grateful to Jack Brisley and Edmund Prager for their contributions to liftfan development and to Judith Farman, Viacheslav Sedunin, Chris Clark, and the rest of the Whittle Laboratory for their helpful thoughts and comments.

Conflict of Interest

There are no conflicts of interest.

Data Availability Statement

The datasets generated and supporting the findings of this article are obtainable from the corresponding author upon reasonable request.

References

[1] Gill, W. J., 1959, "ARD-236 Summary Report," Technical Report AD 225794, Hiller Aircraft Corporation.
[2] Zhang, T., Qiao, G., Smith, D. A., Barakos, G. N., and Kusyumov, A., 2021, "Parametric Study of Aerodynamic Performance of Equivalent Ducted/Un-Ducted Rotors," Aerosp. Sci. Technol., **117**, p. 106984.
[3] Hirono, F. C., Martinez, A. T., Elliott, A. S., Taylor, J. V., Grimshaw, S. D., and Lefas, D., 2022, "Aeroacoustic Design and Optimisation of an All-Electric Ducted Fan Propulsion Module for Low-Noise Impact," 28th AIAA/CEAS Aeroacoustics 2022 Conference, Southampton, UK, June 14–17, p. 3034.
[4] Hine, R. D., Farman, J. R., Grimshaw, S. D., and Taylor, J. V., 2023, "Short Ducted Fan Diffusers With Integral Splitter Blades," In Turbo Expo: Power for Land, Sea, and Air, Vol. 87103, American Society of Mechanical Engineers, p. V13CT33A005.
[5] Smyth, J. M., and Miller, R. J., 2021, "Selecting a Compressor Meridional Topology: Axial, Mixed, Radial," In Turbo Expo: Power for Land, Sea, and Air, Vol. 84928, American Society of Mechanical Engineers, p. V02CT34A013.
[6] Taylor, J. V., and Miller, R. J., 2016, "Competing Three-Dimensional Mechanisms in Compressor Flows," ASME J. Turbomach., **139**(2), p. 021009.
[7] Graf, W., Fleming, J., and Ng, W., 2008, "Improving Ducted Fan UAV Aerodynamics in Forward Flight," 46th AIAA Aerospace Sciences Meeting and Exhibit, Reno, NV, Jan. 7–10, p. 430.
[8] Abrego, A. I., Bulaga, R. W., and Rutkowski, M., 2002, "Performance Study of a Ducted Fan System," American Helicopter Society Aerodynamics, Acoustics and Test and Evaluation Technical Specialists Meeting, San Francisco, CA, Jan. 23–25.
[9] Ohanian, O. J., Gelhausen, P. A., and Inman, D. J., 2012, "Nondimensional Modeling of Ducted-Fan Aerodynamics," J. Aircraft, **49**(1), pp. 126–140.
[10] Yoon, M. K., Jeon, C. S., and Kauh, S. K., 2002, "Efficiency Increase of an Induction Motor by Improving Cooling Performance," IEEE Trans. Energy Conversion, **17**(1), pp. 1–6.
[11] Huang, J., Naini, S. S., Miller, R., Rizzo, D., Sebeck, K., Shurin, S., and Wagner, J., 2019, "A Hybrid Electric Vehicle Motor Cooling System-Design, Model, and Control," IEEE Trans. Vehicular Technol., **68**(5), pp. 4467–4478.
[12] Soparat, J., and Benyajati, C., 2013, "Liquid Cooled Induction Motor: Computational Design, Heat Transfer Analysis, Parametric Study, and Performance Testing," SAE Int. J. Altern. Powertrains, **2**(1), pp. 1–6.
[13] Hu, X., Qian, Y., Yang, B., Dong, C., Zhang, Y., and Zhuge, W., 2023, "Aerodynamic Design of Cooling Guide for Electrical Machine in Electric Ducted Fan," ASME J. Eng. Gas Turbines Power, **145**(5), p. 051009.
[14] Konovalov, D., Tolstorebrov, I., Eikevik, T. M., Kobalava, H., Radchenko, M., Hafner, A., and Radchenko, A., 2023, "Recent Developments in Cooling Systems and Cooling Management for Electric Motors," Energies, **16**(19), p. 7006.
[15] Nathen, P., Strohmayer, A., Miller, R., Grimshaw, S. D., and Taylor, J., 2021, "Architectural Performance Assessment of an Electric Vertical Take-Off And Landing (eVTOL) Aircraft Based on a Ducted Vectored Thrust Concept," Lilium GmbH, Claude-Dornier StraeSSe, Weßling, Germany, Technical Report.
[16] Moore, M., Fei, X., Jedamski, D., Perry, A., Morejon Ramirez, L. A., Villa, I., and Lakshminarayan, V. K., 2023, "Unlocking Low-Cost Regional Air Mobility Through Whisper Aero-Propulsive Coupling," AIAA Aviation 2023 Forum, San Diego, CA, June 12–16, p. 3456.
[17] Horizon Aircraft Inc. 2023 "Aircraft Airfoil Having an Internal Thrust Unit, and Aircraft Having the Same". US11548621B1, US Patent and Trademark Office, Jan. 10, 2023.
[18] Greitzer, E. M., Tan, C. S., and Graf, M. B., 2007, *Internal Flow: Concepts and Applications*, Cambridge University Press, Cambridge, UK.
[19] 2007, "Performance of Circular Annular Diffusers in Incompressible Flow". Technical Report ESDU75026.
[20] Hoerner, S. F., 1965, *Fluid-Dynamic Drag : Practical Information on Aerodynamic Drag and Hydrodynamic Resistance*, Hoerner Fluid Dynamics, Brick Town, NJ.
[21] Abbott, I. H., and Von Doenhoff, A. E., 2012, *Theory of Wing Sections: Including a Summary of Airfoil Data*, Courier Corporation, New York.
[22] Wheeler, P., Sirimanna, T. S., Bozhko, S., and Haran, K. S., 2021, "Electric/Hybrid-Electric Aircraft Propulsion Systems," Proc. IEEE, **109**(6), pp. 1115–1127.

[23] Brandvik, T., and Pullan, G., 2010, "An Accelerated 3D Navier–Stokes Solver for Flows in Turbomachines," ASME J. Turbomach., **133**(2), p. 021025.
[24] Spalart, P., and Allmaras, S., 1992, "A One-Equation Turbulence Model for Aerodynamic Flows," 30th Aerospace Sciences Meeting and Exhibit, Reno, NV, Jan. 6–9, p. 439.
[25] Guo, R. W., and Seddon, J., 1983, "Swirl Characteristics of an S-Shaped Air Intake With Both Horizontal and Vertical Offsets," Aeronaut. Q., **34**(2), pp. 130–146.
[26] Taylor, J. V., Flanagan, F., Dunlop, A., Grimshaw, S. D., and Miller, R. J., 2021, "Super Aggressive S-Ducts for Air Breathing Rocket Engines," ASME J. Turbomach., **143**(6), p. 061015.
[27] Whitaker, S., 1972, "Forced Convection Heat Transfer Correlations for Flow in Pipes, Past Flat Plates, Single Cylinders, Single Spheres, and for Flow in Packed Beds and Tube Bundles," AIChE J., **18**(2), pp. 361–371.
[28] Holman, J. P., 2002, *Heat Transfer*, 9th ed., McGraw Hill, Boston, MA.
[29] Von Backström, T. W., 2005, "A Unified Correlation for Slip Factor in Centrifugal Impellers," ASME J. Turbomach., **128**(1), pp. 1–10.
[30] Siemens, 2021. "STAR-CCM+v2021.1 User Manual".
[31] Klostermeier, C., 2008, "Investigation into the Capability of Large Eddy Simulation for Turbomachinery Design," PhD thesis, University of Cambridge, Cambridge, UK.
[32] Grimshaw, S. D., and Taylor, J. V., 2016, "Fast Settling Millimetre-Scale Five-Hole Probes," Ceramics; Controls, Diagnostics and Instrumentation; Education; Manufacturing Materials and Metallurgy of Turbo Expo: Power for Land, Sea, and Air, Vol. 6, p. V006T05A014.
[33] Cumpsty, N. A., 2004, *Compressor Aerodynamics*, Longman Scientific and Technical, Malabar, FL.
[34] T-MOTOR, 2024. "T-MOTOR F1000-KV300 Specifications".